Article

Conversion of Hard to Soft Magnetic Ferrite Nanowires by Paramagnetic Shielding

Xian-Lin Zeng *, Indujan Sivanesarajah and Uwe Hartmann

Institute of Experimental Physics, Saarland University, D-66123 Saarbrücken, Germany;
indujan.sivanesarajah@uni-saarland.de (I.S.); u.hartmann@mx.uni-saarland.de (U.H.)
*   Correspondence: mophiese@gmail.com

Abstract: In this study, we investigate the magnetization behavior of coaxial nanowires fabricated through the sol-gel electrospinning method. Our analysis uncovers a significant reduction in coercivity for $CoFe_2O_4$ nanowires when $BaTiO_3$ is used as the shell material, effectively transforming them from hard to soft magnetic. This intriguing behavior is attributed to the magnetization reversal effect at the interface between ferromagnetic and paramagnetic regions, and it is also observed in $NiFe_2O_4$ and Fe_2O_3 nanowires. Surprisingly, introducing a $GdBa_2Cu_3O_7$ shell induces a similar effect. Additionally, we employ magnetic impedance measurements on the coaxial nanowires, unveiling their potential for magnetic field sensing applications.

Keywords: electrospinning; core-shell structure; coaxial nanowire; ferrite; magnetic reversal

1. Introduction

As a class of materials renowned for their unique blend of physical properties, chemical stability, and cost-effectiveness, ferrites have gained increasing popularity across a wide range of applications [1–4]. Among these, $CoFe_2O_4$ stands out with its mixed cubic spinel structure (Fd3m space group), occupying a distinctive position between soft and hard magnetic ferrites and often classified as a semi-hard material. The emergence of nanotechnology has further enriched the properties of ferrites, leading to the application of nanocrystalline $CoFe_2O_4$ in magnetic recording, magnetic fluids, magnetic drug delivery, sensors, electrical devices, optoelectronics, and photocatalytic activities, among others [5–8]. Researchers have achieved high coercivity and saturation magnetization in nanocrystalline $CoFe_2O_4$ by introducing doping with various transition metals into its host spinel ferrite structure [9–15]. The $CoFe_2O_4$ anisotropic particles with size between 5.1 and 12.5 nm have been reported showcasing superparamagnetic behavior [16]. Such nano-sized ferrites have utility in magnetic data storage, magnetic imaging, and microwave devices [17,18].

In the realm of multiferroic systems, the $CoFe_2O_4$@$BaTiO_3$ system (The compound comprises $CoFe_2O_4$ as the core material positioned before the '@' symbol, and $BaTiO_3$ as the shell material positioned after the '@' symbol.) has garnered significant attention, attracting fundamental research and applications in novel memory devices and magnetic field sensors [19–23]. Coercivity in $CoFe_2O_4$@$BaTiO_3$ materials is influenced by the size of $CoFe_2O_4$ particles and the magnetic dipolar interactions between them. For instance, when the particles are within the superparamagnetic size limit and fully isolated by $BaTiO_3$, a low coercivity of 15 Oe can be achieved [24]. On the other hand, core-shell $CoFe_2O_4$@$BaTiO_3$ particles, with sizes between 40 and 60 nm, exhibit higher coercivity (264 Oe), while the core-shell $CoFe_2O_4$@$BaTiO_3$ nanotubes (diameter around 100 nm) exhibit comparable coercivity to pure $CoFe_2O_4$ nanotubes, reaching 901 Oe [21].

In this study, we present intriguing results obtained from coaxial electrospun $CoFe_2O_4$@$BaTiO_3$ nanowires with an average diameter over 200 nm, revealing unexpected soft magnetism compared to the relatively hard magnetic behavior observed in pure

$CoFe_2O_4$ nanowires. This behavior cannot be solely attributed to superparamagnetic effects as observed in isolated $CoFe_2O_4$ particles. To gain insight into this magnetism variation, we investigate the influence of core and shell materials in coaxial nanowires and provide possible explanation about this phenomenon through the lens of magnetic reversal mechanisms [25,26]. Additionally, magnetic impedance measurements are applied to the aligned coaxial nanowires, demonstrating their potential application in magnetic field sensing. These findings shed light on the intriguing properties of coaxial $CoFe_2O_4@BaTiO_3$ nanowires and hold promise for future magnetic sensing applications.

2. Materials and Methods

2.1. Preparation of Coaxial Nanowires

The fabrication of all the nanowires is achieved through the sol-gel electrospinning method, employing commercially available chemicals from Alfa Aesar GmbH (Ward Hill, MA, USA). All the chemicals are above analytical grade. To prepare the $CoFe_2O_4$ precursor, cobalt acetate $(Co(CH_3COO)_2 \cdot 4H_2O)$ and iron nitrite $(Fe(NO)_3 \cdot 9H_2O)$ are weighted in the molar ratio Co:Fe = 1:2 and dissolved in deionized water, the polymer polyvinylpyrrolidone (PVP) (MW 130,000) is then mixed with solution as to increase the viscosity of the precursor, preparing for the following electrospinning process. Table 1 listed the precursor recipes of all the required chemical phases in this work.

Table 1. List of precursor recipes for the required chemical phase in this work. P.S.:M.R. indicates 'Molar Ratio'.

Phase	Chemicals			M.R.			Solvent
$CoFe_2O_4$	$Co(Ac)_2 \cdot 4H_2O$	$Fe(NO)_3 \cdot 9H_2O$		1	2		water
$NiFe_2O_4$	$Ni(Ac)_2 \cdot 4H_2O$	$Fe(NO)_3 \cdot 9H_2O$		1	2		water
Fe_2O_3		$Fe(NO)_3 \cdot 9H_2O$		-			water
$BaTiO_3$	$Ba(Ac)_2$	$Ti(C_16H_{36}O_4)$		1	1		Propionic acid
$GdBa_2Cu_3O_7$	$Gd(Ac)_3 \cdot xH_2O$	$Ba(Ac)_2$	$Cu(Ac)_2$	1	2	3	Propionic acid

To fabricate coaxial nanowires, we utilize a specially designed electrospinning setup, as shown in Figure 1A. During the electrospinning process, the core precursor and shell precursor are housed in separate syringes, both driven by the same microspeed boost pump. The syringes are coupled to a coaxial nozzle (Figure 1B). When the two different precursors emerge at the end of the nozzle, they form a core-shell liquid sphere as shown in (Figure 1C). Upon applying high voltage to the outer nozzle, the core-shell sphere becomes ionized and morphs into a coaxial jet under the influence of the electric field force between the high voltage nozzle and the grounding collector. Consequently, the coaxial fibers are drawn and collected on the collector. Subsequent thermal treatment at 650 °C yields the desired phase configuration in the coaxial nanowires.

2.2. Sample Preparation for the Magnetic Impedance Measurement

Typically, the collected electrospun nanowires are randomly distributed. To conduct magnetic impedance measurements on these nanowires, it becomes necessary to align them. This alignment can be accomplished through the electric field distribution on the collection area of the electrospinning setup. Two vertical supports are affixed to the grounded collector. Owing to the disparity in vertical positions between the upper extremity of the support and the plane of collection, the electrostatic field undergoes a rearrangement as illustrated in Figure 2A. This rearrangement prompts the emergence of a lateral force within the region encompassing the upper portions of the supports, inducing the alignment of charged fibers in consonance with the lateral force vector, as depicted in Figure 2B. Subsequent, employing a silicon wafer positioned in alignment with the direct path connecting the two supports, it is foreseeable that the orientation of the silicon wafer's plane will coincide with the

established fiber alignment. Consequently, the act of 'gathering' the fibers possessing the desired alignment becomes achievable (as shown in Figure 2D) through the adhesion of the wafer to the fibers.
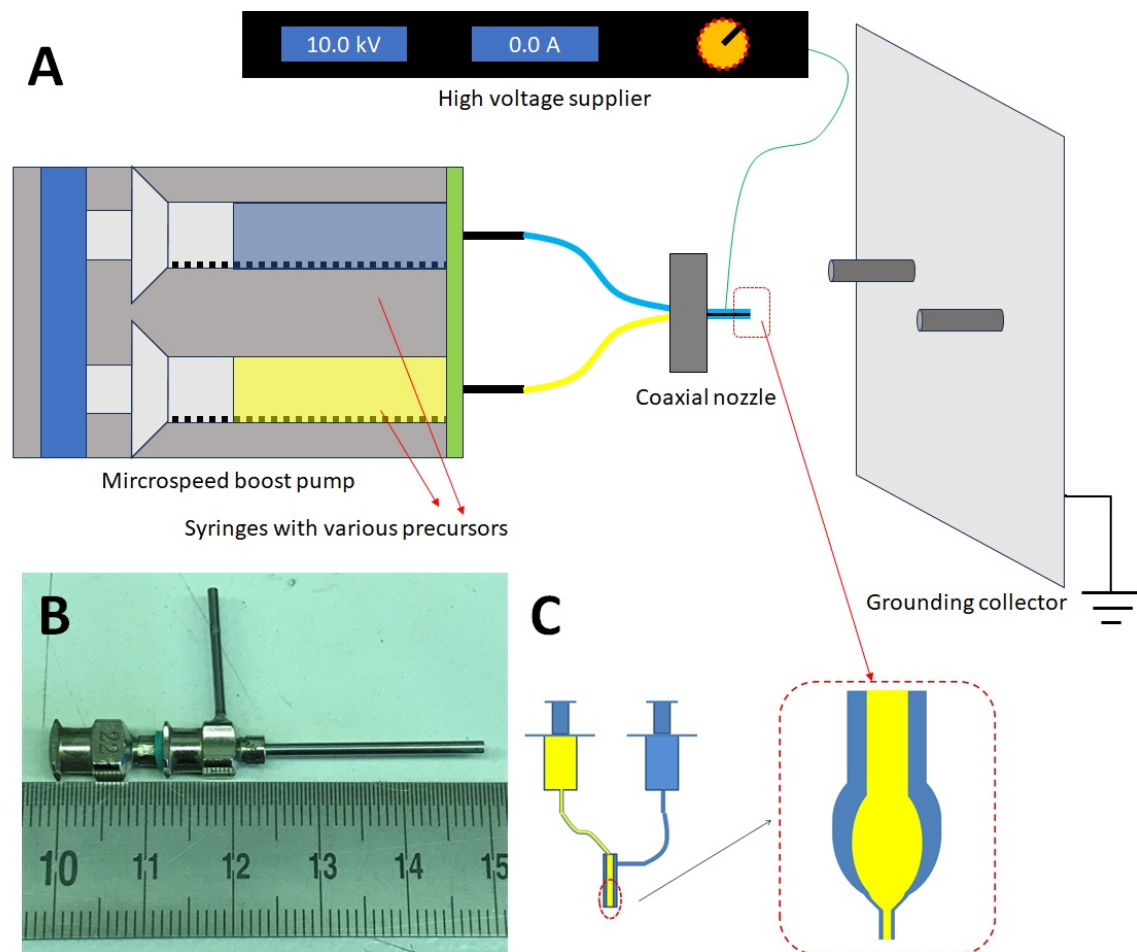
Figure 1. (**A**) Scheme of coaxial electrospinning setup; (**B**) Image of the coaxial electrospinning nozzle; (**C**) Scheme of the formation process of coaxial fiber.

In the subsequent stage, we employ Laser lithography (μpg 101 from Heidelberg Instruments) to write an electric connection pattern on the aligned nanowires. Due to the precise alignment of the nanowires, when we overlay the electrode onto the nanowires with matching orientation, it is possible that the electrodes uniformly draping over the parallel nanowires, avoiding any form of nanowire intersection. It's even conceivable for a solitary nanowire to align itself between the electrodes. This simplified arrangement facilitates subsequent analysis in contrast to the intricate network of nanowires. Subsequently, a 300 nm copper layer is deposited by sputtering on the nanowires to form electrodes in the pattern shown in Figure 3. The electrodes contact the ends of the nanowire (Given the discernible difference in size between the electrode and the nanowire, as illustrated in the inset image, we introduce dashed lines to indicate the precise nanowire location).

To conduct magnetic impedance measurements on the nanowires, we utilize a vector analyzer (Rohde und Schwarz ZNL-3) featuring a three-pin connection. According to this setup, the upper part of the electrode serves as the ground connection, while the bottom part is designated for the source connection.
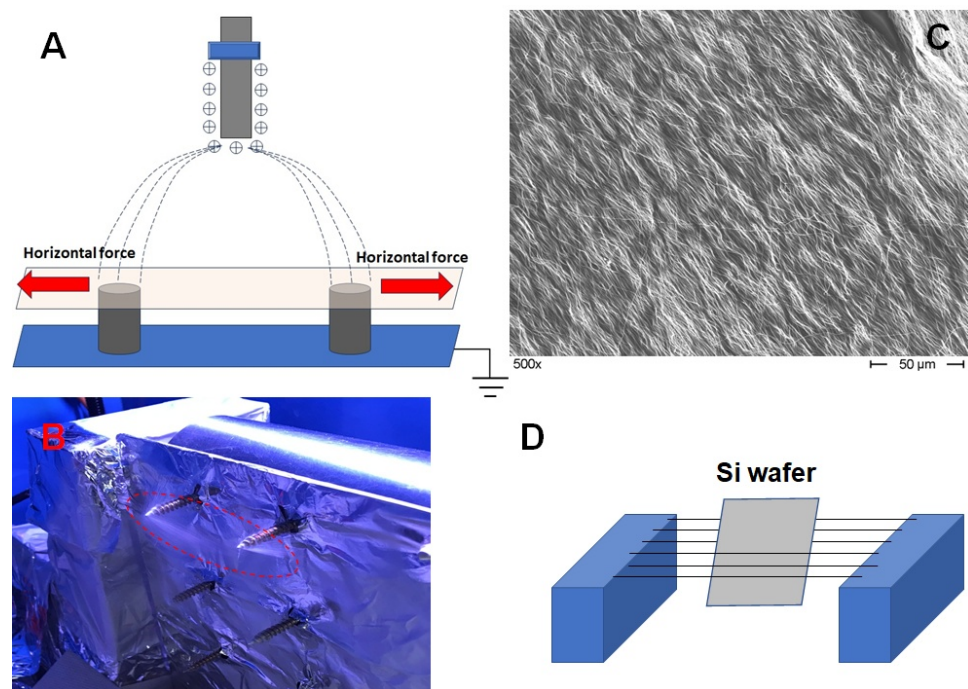
Figure 2. (**A**) collection setup for aligned nanowires; (**B**) Image of the practical collection setup, the highlight area shows the collected fibers with specific orientation; (**C**) SEM image of the aligned nanowreis; (**D**) approach of transporting aligned nanowires to a silicon wafer.
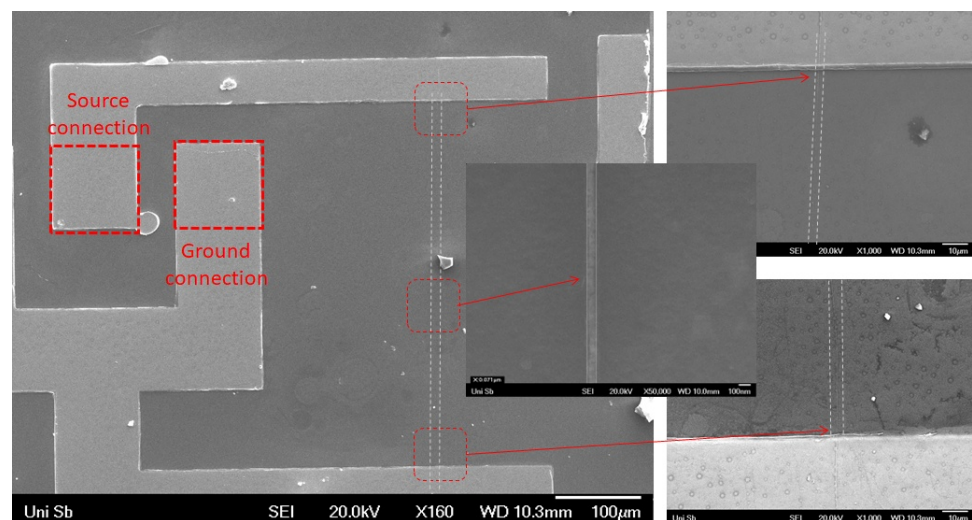
Figure 3. SEM of the nanowire with electrode for magnetic impedance measurement.

2.3. Remaining Experimental Details

The chemical phases of the samples were identified using a high-resolution automated RINT2200 X-ray powder diffractometer (Rigaku smart-lab, Wilmington, MA, USA) with Cu-K$_\alpha$ radiation (40 kV, 40 mA, $\lambda_{k_{\alpha1}}$ = 1.5406 Å, $\lambda_{k_{\alpha2}}$ = 1.5444 Å). The microstructure characterization involved SEM imaging with a Hitachi S800 (Hitachi, Tokyo, Japan) at 10 kV and TEM analysis using JEOL JSM-7000 F (JEOL, Tokyo, Japan) with 200 kV and LaB$_6$ cathode, which also included EDAX element analysis. For magnetic property characterization, the samples were examined via PPMS (Quantum Design 6000 (Quantum Design, San Diego, CA, USA)).

3. Results and Discussion

3.1. Microstructure of the Samples

To evaluate the suitability of the coaxial nozzle for coaxial nanowire fabrication, we initially utilized $BaTiO_3$ precursor as the shell material, while the core precursor consisted of a mixture of PVP and propionic acid. As illustrated in Figure 4A, the organic component underwent decomposition and evaporation during the thermal treatment, resulting in the formation of $BaTiO_3$ nanotubes with the desired perfect shape. In comparison, the $CoFe_2O_4@BaTiO_3$ coaxial nanowires exhibit a completely solid appearance as shown in Figure 4B. Both the $BaTiO_3$ nanotubes and $CoFe_2O_4@BaTiO_3$ coaxial nanowires have average diameters of approximately 200 nm. According to the analysis of the XRD refinement data and the observation from TEM, the average grain size of the coaxial nanowires ranges from 20 nm to 50 nm. The grain size appears to be excessively large to sustain superparamagnetism [16].
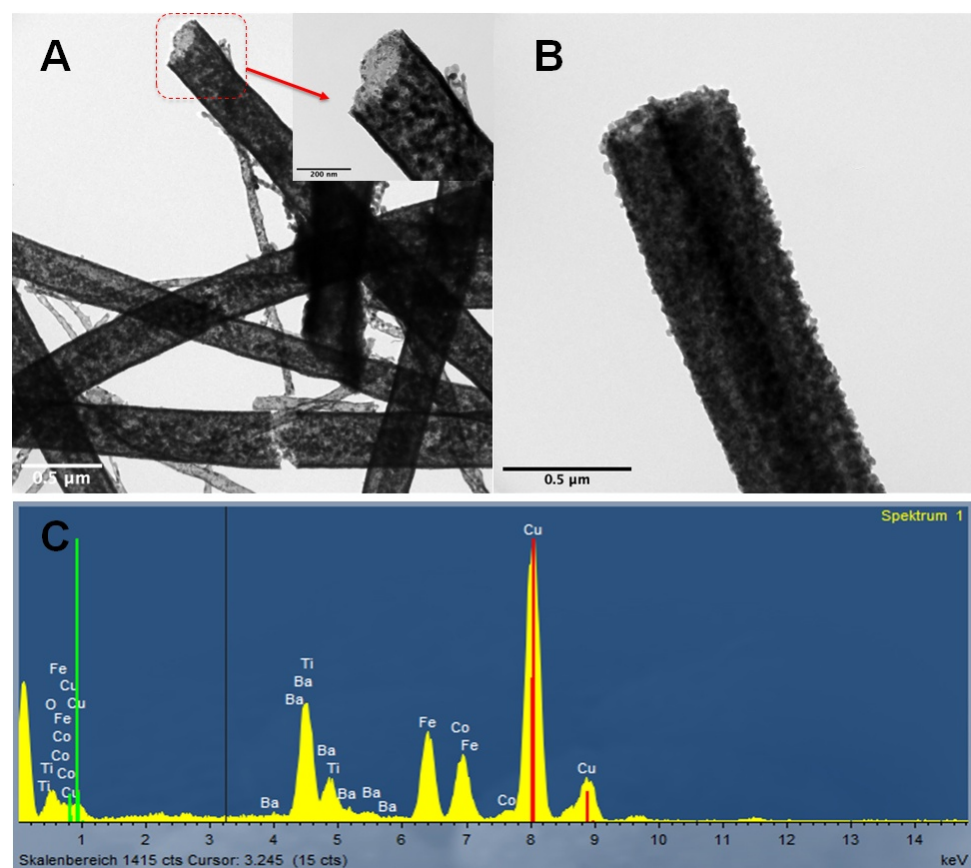
Figure 4. (**A**) TEM image of the $BaTiO_3$ nanotubes; (**B**) TEM image of the $CoFe_2O_4@BaTiO_3$ coaxial nanowire; (**C**) EDAX analysis of the $CoFe_2O_4@BaTiO_3$ coaxial nanowire. The red and green peaks display the main and subordinate peaks of Cu element from the TEM holding grid.

3.2. Phase Analysis of the Coaxial Nanowires

Figure 4C displays the EDAX analysis results of the coaxial nanowires, indicating an atomic ratio of Co:Fe:Ba:Ti = 16.23:30.35:28.02:25.40. This confirms the presence of both $CoFe_2O_4$ and $BaTiO_3$ phases in the coaxial nanowires, with an approximate molar ratio of 1:2. Furthermore, Figure 5 presents the XRD pattern of the coaxial nanowires, providing additional evidence for the existence of both $CoFe_2O_4$ and $BaTiO_3$ phases. The XRD refinement analysis reveals a mass ratio between the two phases as 22.52:77.48, which, when converted to a molar ratio, becomes 22.41:77.59. The higher ratio of $BaTiO_3$ phase can be attributed to its shell configuration on the nanowires, as the XRD diffraction signals

mainly originate from the surface. Considering this aspect, the phase ratio estimated from EDAX analysis is deemed more reliable.
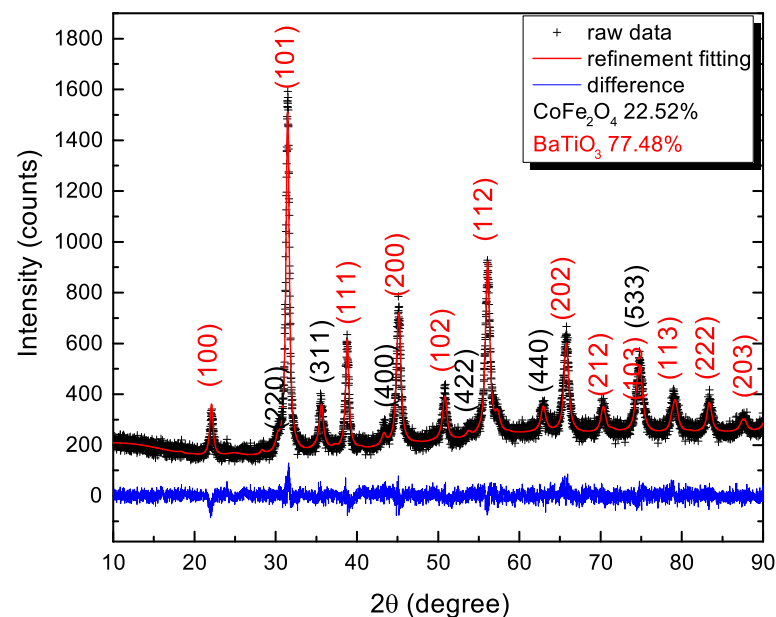
Figure 5. XRD of the $CoFe_2O_4@BaTiO_3$ coaxial nanowires with XRD refinement and phase analysis.

3.3. Magnetic Properties of the Samples

Figure 6A illustrates the M(*H*) magnetization loop of the pure $CoFe_2O_4$ nanowires at 295 K, exhibiting a coercivity (H_C) of 468 Oe, with the saturation field at 4700 Oe. When compared to the electrospun $CoFe_2O_4$ nanowires from another study [27], the coercivity of these nanowires is relatively lower, possibly due to lattice defects induced during the thermal treatment. Nevertheless, these nanowires still fall into the category of 'hard magnetic' materials.

Figure 6B illustrates the M(*H*) magnetization loop of pure $BaTiO_3$ nanowires at 295 K. Initially, a pronounced paramagnetic signal is noticeable. Upon a more detailed examination at lower external magnetic fields, a subtle ferromagnetic component becomes evident. This behavior is of particular interest due to previous reports indicating the presence of ferromagnetic order within nanoscale $BaTiO_3$ [28,29]. This ferromagnetism is ascribed to intrinsic defects, which gain prominence in smaller grain sizes. Studies in [29], focused on $BaTiO_3$ nanoparticles with an average size of approximately 21 to 24 nm, have highlighted this phenomenon. Our $BaTiO_3$ nanottubes, as observed through TEM, exhibit an average grain size of around 20 nm. As a result, we attribute the observed weak ferromagnetic behavior in our $BaTiO_3$ nanotubes to the emergence of lattice defects within grains during the thermal treatment, as the as-prepared fibers transform into inorganic fibers. However, as a general assumption, we maintain the notion that $BaTiO_3$ nanotubes exhibit paramagnetism in magnetic measurements.

Surprisingly, a striking transformation occurs when a paramagnetic shell of $BaTiO_3$ is introduced. As depicted in Figure 6C, the coercivity of the $CoFe_2O_4@BaTiO_3$ coaxial nanowires reduces significantly to 5 Oe, and the saturation field is now at 495 Oe. In essence, the incorporation of a $BaTiO_3$ shell causes a shift from hard magnetic to soft magnetic behavior in the $CoFe_2O_4$ nanowires.

As previously discussed, the reduction of coercivity in these coaxial nanowires cannot be explained solely by the superparamagnetic effect. Instead, the $CoFe_2O_4@BaTiO_3$ coaxial nanowire can be seen as a multilayer system, with paramagnetic (PM) layers ($BaTiO_3$) at the top and bottom, and a ferromagnetic (FM) layer ($CoFe_2O_4$) at the center. When an external magnetic field is applied to the system, the magnetizations of the different layers align parallel to the field direction. However, when the external magnetic field opposes the

magnetization of the FM region, the PM region develops a magnetic moment proportional to its susceptibility. These induced moments decay exponentially with distance away from the interfaces [25]. In this configuration, the magnetization of the FM region becomes antiparallel to the induced PM magnetization. Such a setup is energetically unfavorable, leading to an increase in the interlayer exchange energy. Interestingly, this energy facilitates the magnetization reversal process of the FM region, favoring the parallel alignment of the magnetizations of the PM and FM regions. Consequently, a reduction in the coercivity field is observed. Based on this analysis, it becomes evident that the interface energy plays a crucial role in assisting the magnetization reversal process of the FM region, especially when the magnetization of the FM region and the external magnetic field are opposite to each other.

For comparison, we attempted to exchange the core material to $BaTiO_3$ while the shell material became $CoFe_2O_4$, resulting in a coercivity (H_C) of 79 Oe for the new coaxial nanowires as shown in Figure 6D. The reduction of coercivity still persists, although it is not as pronounced as in the previous configuration. This is attributed to the system transforming into an FM/PM/FM multilayer setup, where the magnetization reversal process is constrained by the presence of the shell FM layer.
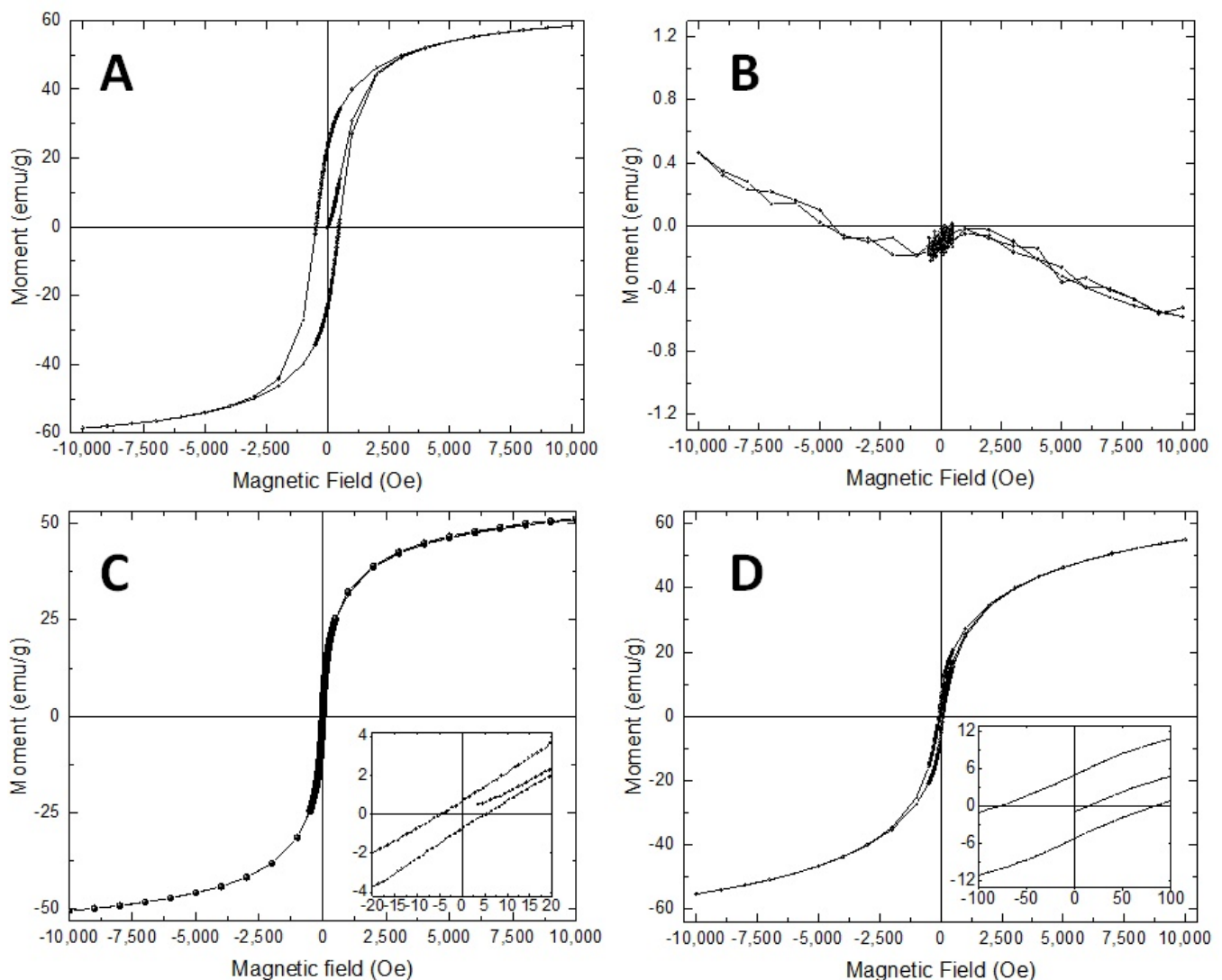
Figure 6. M(H) magnetization of nanowires at 295 K: (**A**) $CoFe_2O_4$ nanowires; (**B**) $BaTiO_3$ nanotubes; (**C**) $CoFe_2O_4$@$BaTiO_3$ coaxial nanowires; (**D**) $BaTiO_3$@$CoFe_2O_4$ coaxial nanowires.

In our further investigation, we sought to understand the magnetization behavior of the coaxial nanowires as we varied the phase ratio. Achieving this was simple by decreasing the $BaTiO_3$ concentration in the corresponding precursor. Figure 7 presents the magnetization results of the coaxial nanowires with different phase ratios. When $CoFe_2O_4$:$BaTiO_3$ = 1:1 (Figure 7A), the coercivity of the samples remained small at H_C = 6.7 Oe. However, this value increased to 146.3 Oe when the molar ratio of the $BaTiO_3$ phase was halved. This observation indicates that as the ratio of the $BaTiO_3$ phase decreases, the magnetization reversal effect from the FM/PM interface weakens progressively. This explains why in the work of Raidongia et al., the coaxial nanowires synthesized via hydrothermal treatment exhibited a coercivity comparable to pure $CoFe_2O_4$ nanowires [21]. The low ratio of $BaTiO_3$ phase led to the absence of the magnetization reversal effect.
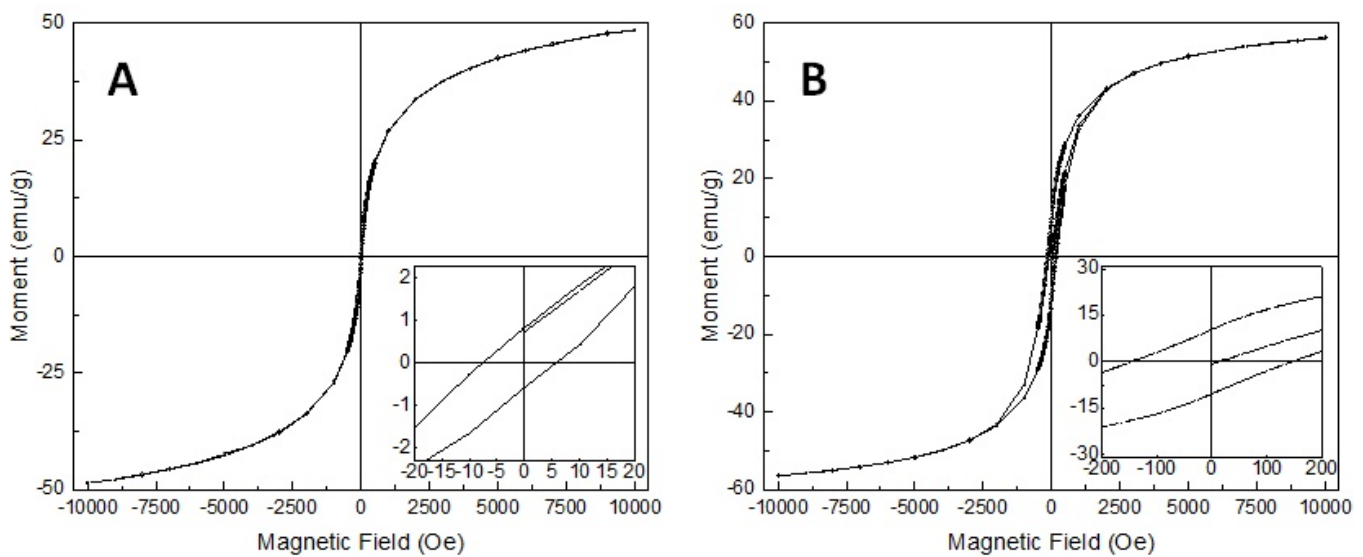
Figure 7. M(H) magnetization of $CoFe_2O_4$@$BaTiO_3$ coaxial nanowires with different phase ratio: (**A**) $CoFe_2O_4$:$BaTiO_3$ = 1:1; (**B**) $CoFe_2O_4$:$BaTiO_3$ = 2:1.

In the subsequent stage, we aimed to investigate whether the magnetization reversal effect was specific to $CoFe_2O_4$@$BaTiO_3$ coaxial nanowires or not. To explore this, we replaced the core material of $CoFe_2O_4$ with $NiFe_2O_4$ and Fe_2O_3, and then measured the magnetization behavior of the newly formed coaxial nanowires. As depicted in Figure 8A–D, the $NiFe_2O_4$ nanowires exhibited a coercivity of 210 Oe. However, upon adding a $BaTiO_3$ shell, the coercivity reduced significantly to 9.5 Oe. A similar trend was observed with the Fe_2O_3 nanowires, where the coercivity decreased from 133 Oe to 8.5 Oe after incorporating a $BaTiO_3$ shell.

Through occasional attempts, we made an intriguing discovery that $BaTiO_3$ is not the sole material capable of serving as the paramagnetic (PM) layer for magnetization reversal in the coaxial nanowire system. As demonstrated in Figure 8E, a noticeable reduction in coercivity also occurs with the $GdBa_2Cu_3O_7$ shell (H_C = 48 Oe). At 5 K, the hysteresis loop of the $CoFe_2O_4$@$GdBa_2Cu_3O_7$ coaxial nanowires displays a ferromagnetic loop. However, it is evident that the shape of the hysteresis loop is influenced by the superconducting component, as shown in the inset of Figure 8F.
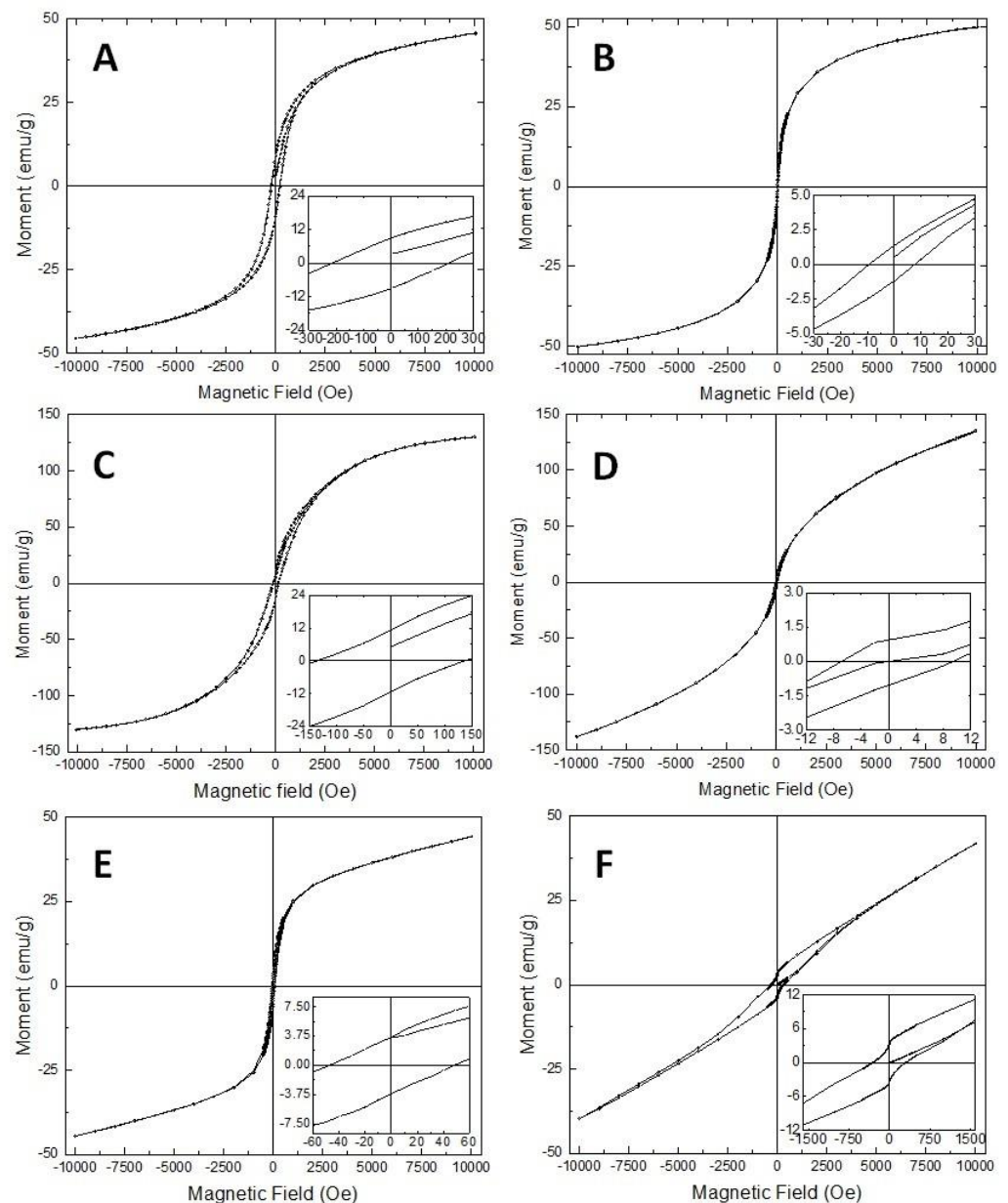
Figure 8. (**A–D**): M(H) magnetization of ferrite nanowires and their corresponding coaxial nanowires: (**A**) NiFe$_2$O$_4$ nanowire, (**B**) NiFe$_2$O$_4$@BaTiO$_3$ coaxial nanowires, (**C**) Fe$_2$O$_3$ nanowires, (**D**) Fe$_2$O$_3$@BaTiO$_3$ coaxial nanowires; (**E,F**): M(H) magnetization of CoFe$_2$O$_4$@GdBa$_2$Cu$_3$O$_7$ coaxial nanowires: (**E**): 295 K; (**F**): 5 K.

3.4. Magnetic Impedance Measurement of the Coaxial Nanowires

Figure 9 illustrates the magnetic impedance results of the CoFe$_2$O$_4$@BaTiO$_3$ coaxial nanowires across the frequency range from 10 MHz to 3 GHz. At 20 MHz, a single peak emerges with a maximum at 57.5 Oe, and the ratio increases with frequency up to 370% at 3 GHz. Another peak appears at 40 MHz, reaching a maximum at −53.8 Oe, and its ratio increases with frequency up to 77% at 3 GHz.

Consider a sample with its magnetic easy axis oriented along the wire's length. In this context, applying both the current and magnetic field along the wire results in a singular peak. This outcome is a consequence of the peak transverse permeability emerging at H = 0. Conversely, in the opposite scenario where the magnetization stands perpendicular to the wire's length, while the current is parallel to the wire, a double peak pattern emerges. This

phenomenon finds its peak at the anisotropy field. These two peaks correspond to the ferromagnetic resonances, manifesting in both the saturated and non-saturated states [30]. When an angle between the field and the magnetic easy axis exists, the magnetization undertakes a rotation in alignment with this angle. This rotation precipitates an impedance increase.

In our experimental setup, the magnetic field is applied perpendicular to the electric connection pattern. The small misalignment of the nanowire (not precisely perpendicular to the connected pattern (as shown in right images of Figure 3)) causes an angle between the current and external field. The lateral component of the magnetization in relation to the current induces the appearance of a secondary peak. The asymmetry in the experimental peak heights can be attributed to the presence of non-diagonal components within the impedance tensor, as clarified in [30]. Moreover, since the wire is not field treated, the magnetization becomes randomly oriented.

In conclusion, the nanowires exhibit a high Giant Magnetoimpedance (GMI) ratio that can be utilized for magnetic field sensing. However, the preferred configuration is the double peak, as the linear range between those two peaks can be employed. To achieve this, the following strategies can be employed: 1. Preparing the nanowires with an external field perpendicular to the length dimension during heat treatment. This approach amplifies the lateral component of magnetization, rendering the impedance more conducive to the emergence of double peaks; 2. Inducing helical anisotropy through joule heating. This technique prevents the magnetic hardening often observed during traditional furnace annealing, facilitating substantial enhancement in GMI performance [31].
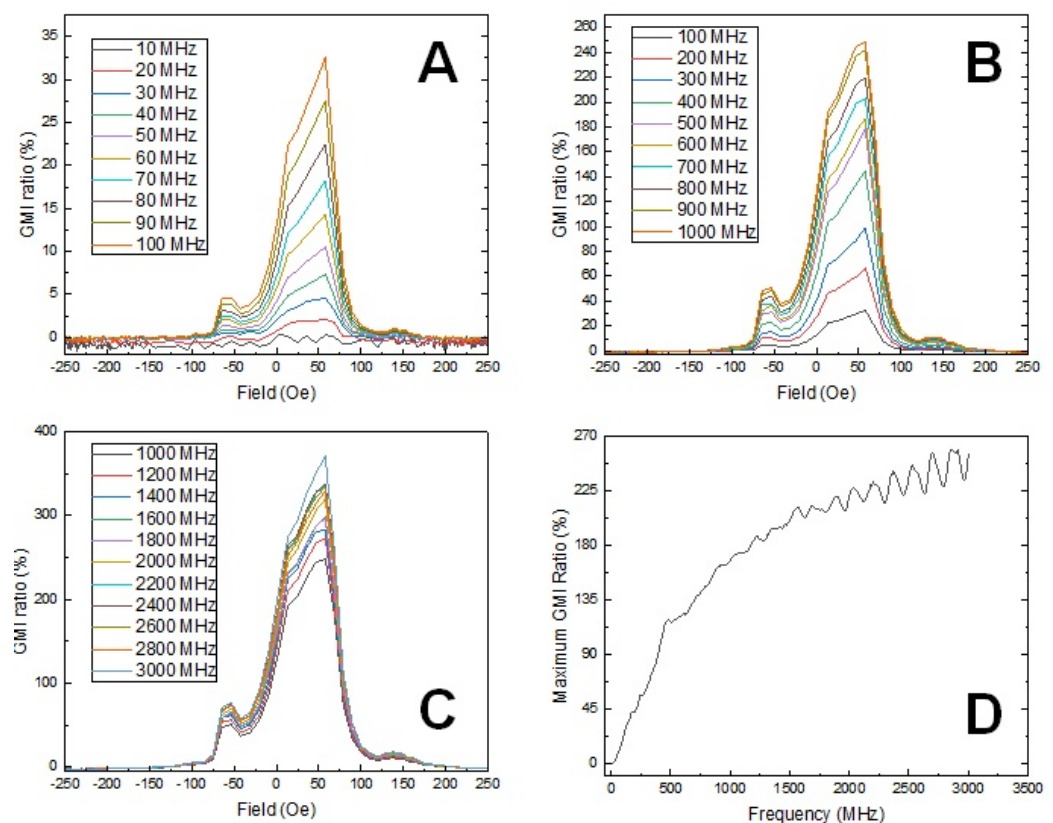
Figure 9. (**A–C**): Magnetic impedance measurement of the $CoFe_2O_4$@$BaTiO_3$ coaxial nanowires: (**A**) 10 MHz–100 MHz, (**B**) 100 MHz–1 GHz, (**C**) 1 GHz–3 GHz; (**D**) Maximum GMI ratio dependance on frequency.

4. Conclusions

In this study, we investigated the magnetization behavior and properties of $CoFe_2O_4$@$BaTiO_3$ coaxial nanowires, along with their variations when different core materials were used. Our findings revealed a remarkable reduction in coercivity when a

BaTiO$_3$ shell was introduced to the CoFe$_2$O$_4$ core, leading to a shift from hard magnetic to soft magnetic behavior. This intriguing magnetization reversal effect was also observed when GdBa$_2$Cu$_3$O$_7$ was used as the shell material. Additionally, we explored the impact of different phase ratios on the coercivity, further validating the significance of the PM layer in the nanowires' magnetic behavior.

Moreover, we discovered that the misalignment of the nanowire affected the observed magnetic impedance behavior, leading to the emergence of multiple peaks. We suggested possible approaches, such as external field treatment or inducing helical anisotropy, to optimize the configuration and utilize the double peak for magnetic field sensing.

Throughout the investigation, our research sheds light on the versatile characteristics of coaxial nanowires and their promising applications, especially in the realm of magnetic field sensing.

Author Contributions: Conceptualization, X.-L.Z.; methodology, X.-L.Z.; validation, U.H.; investigation, X.-L.Z., I.S.; resources, U.H.; data curation, X.-L.Z.; writing–original draft preparation, X.-L.Z.; supervision, U.H. All authors have read and agreed to the published version of the manuscript.

Data Availability Statement: The data that support the findings of this study are available from the corresponding author, [Xian-Lin Zeng], upon reasonable request.

Conflicts of Interest: The authors declare no conflict of interest.

References

1. Jin, S.; Tiefel, T.H.; McCormack, M.; Fastnacht, R.A.; Ramesh, R.; Chen, L.H. Thousandfold change in resistivity in magnetoresistive La-Ca-Mn-O films. *Science* **1994**, *264*, 413–415. [CrossRef] [PubMed]
2. Rodriguez, L.M.; Attfield, J.P. Cation disorder and size effects in magnetoresistive manganese oxide perovskites. *Phys. Rev. B* **1996**, *54*, R15622–R15625. [CrossRef] [PubMed]
3. Ramirez, A.P. Colossal magnetoresistance. *J. Phys. Condens. Matter* **1997**, *9*, 8171–8199. [CrossRef]
4. Mathew, D.S.; Juang, R.-S. An overview of the structure and magnetism of spinel ferrite nanoparticles and their synthesis in microemulsions. *Chem. Eng. J.* **2007**, *129*, 51–65. [CrossRef]
5. Naseri, M.G.; Saion, E.B.; Ahangar, H.A.; Shaari, A.H.; Hashim, M. Simple Synthesis and Characterization of Cobalt Ferrite Nanoparticles by a Thermal Treatment Method. *J. Nanomater.* **2010**, *2010*, 907686.
6. Patil, D.R.; Chougule, B.K. Effect of copper substitution on electrical and magnetic properties of NiFe$_2$O$_4$ ferrite. *Mater. Chem. Phys.* **2009**, *117*, 35–40. [CrossRef]
7. Fan, H.M.; Yi, J.B.; Yang, Y.; Kho, K.W.; Tan, H.R.; Shen, Z.X.; Ding, J.; Sun, X.W.; Olivo, M.C.; Feng, Y.P. Single-Crystalline MFe$_2$O$_4$ Nanotubes/Nanorings Synthesized by Thermal Transformation Process for Biological Applications. *ACS Nano* **2009**, *3*, 2798–2808. [CrossRef]
8. Laokul, P.; Arthan, S.; Maensiri, S.; Swatsitang, E. Magnetic and Optical Properties of CoFe2O4 Nanoparticles Synthesized by Reverse Micelle Microemulsion Method. *J. Supercond. Nov. Magn.* **2015**, *28*, 2483–2489. [CrossRef]
9. Koseoglu, Y.; Alan, F.; Tan, M.; Yilgin, R.; Ozturk, M. Low temperature hydrothermal synthesis and characterization of Mn doped cobalt ferrite nanoparticles. *Ceram. Int.* **2012**, *38*, 3625–3634. [CrossRef]
10. Bhame, S.D.; Joy, P.A. Tuning of the magnetostrictive properties of CoFe$_2$O$_4$ by Mn substitution for Co. *J. Appl. Phys.* **2006**, *100*, 113911. [CrossRef]
11. Koseoglu, Y.; Baykal, A.; Gozuak, F.; Kavas, H. Structural and magnetic properties of Co$_x$Zn$_{1-x}$Fe$_2$O$_4$ nanocrystals synthesized by microwave method. *Polyhedron* **2009**, *28*, 2887–2892. [CrossRef]
12. Kasapoglu, N.; Birsoz, B.; Baykal, A.; Koseoglu, Y.; Toprak, M.S. Synthesis and magnetic properties of octahedral ferrite Ni$_x$Co$_{1-x}$Fe$_2$O$_4$ nanocrystals. *Cent. Eur. J. Chem.* **2007**, *5*, 570–580.
13. Moradmard, H.; Farjami Shayesteh, S.; Tohidi, P.; Abbas, Z.; Khaleghi, M. Structural, magnetic and dielectric properties of magnesium doped nickel ferrite nanoparticles. *J. Alloys Compd.* **2015**, *650*, 116–122. [CrossRef]
14. Zhou, B.; Zhang, Y.W.; Liao, C.S.; Yan, C.H. Magnetism and phase transition for CoFe$_{2-x}$Mn$_x$O$_4$ nanocrystalline thin films and powders. *J. Magn. Magn. Mater.* **2002**, *247*, 70–76. [CrossRef]
15. Chae, K.P.; Lee, J.-G.; Kweon, H.S.; Lee, Y.B. The crystallographic, magnetic properties of Al, Ti doped CoFe$_2$O$_4$ powders grown by sol-gel method. *J. Magn. Magn. Mater.* **2004**, *283*, 103–108. [CrossRef]
16. Virden, A.; Wells, S.; O'Grady, K. Physical and magnetic properties of highly anisotropic cobalt ferrite particles. *J. Magn. Magn. Mater.* **2007**, *316*, e768–e771. [CrossRef]
17. Mahmoudi, M.; Sant, S.; Wang, B.; Laurent, S.; Sen, T. Superparamagnetic iron oxide nanoparticles (SPIONs): Development, surface modification and applications in chemotherapy. *Adv. Drug Deliv. Rev.* **2011**, *63*, 24–46. [CrossRef]

18. Lu, X.; Liang, G.; Sun, Q.; Yang, C. High-frequency magnetic properties of Ni-Zn ferrite nanoparticles synthesized by a low temperature chemical method. *Mater. Lett.* **2011**, *65*, 674–676.

19. Zheng, H.; Wang, J.; Lofland, S.E.; Ma, Z.; Mohaddes-Ardabili, L.; Zhao, T.; Salamanca-Riba, L.; Shinde, S.R.; Ogale, S.B.; Bai, F.; et al. Multiferroic $BaTiO_3$-$CoFe_2O_4$ Nanostructures. *Science* **2004**, *303*, 661–663. [CrossRef]

20. Duong, G.V.; Groessinger, R. Effect of preparation conditions on magnetoelectric properties of $CoFe_2O_4$–$BaTiO_3$ magnetoelectric composites. *J. Magn. Magn. Mater.* **2007**, *316*, e624–e627. [CrossRef]

21. Raidongia, K.; Nag, A.; Sundaresan, A.; Rao, C.N.R. Multiferroic and magnetoelectric properties of core-shell $CoFe_2O_4@BaTiO_3$ nanocomposites. *Appl. Phys. Lett.* **2010**, *97*, 062904. [CrossRef]

22. Lu, X.; Kim, Y.; Goetze, S.; Li, X.; Dong, S.; Werner, P.; Alexe, M.; Hesse, D. Magnetoelectric Coupling in Ordered Arrays of Multilayered Heteroepitaxial $BaTiO_3$/$CoFe_2O_4$ Nanodots. *Nano Lett.* **2011**, *11*, 3202–3206. [CrossRef] [PubMed]

23. Bauer, M.J.; Wen, X.; Tiwari, P.; Arnold, D.P.; Andrew, J.S. Magnetic field sensors using arrays of electrospun magnetoelectric Janus nanowires. *Microsyst. Nanoeng.* **2018**, *4*, 37. [CrossRef] [PubMed]

24. Erdem, D.; Bingham, N.S.; Heiligtag, F.J.; Pilet, N.; Warnicke, P.; Vaz, C.A.F.; Shi, Y.; Buzzi, M.; Rupp, J.L.M.; Heyderman, L.J.; et al. Nanoparticle-Based Magnetoelectric $BaTiO_3$–$CoFe_2O_4$ Thin Film Heterostructures for Voltage Control of Magnetism. *ACS Nano* **2016**, *10*, 9840–9851. [CrossRef]

25. Fallarino, L.; Quintana, M.; Rojo, E.L.; Berger, A. Suppression of Coercivity in Nanoscale Graded Magnetic Materials. *Phys. Rev. Appl.* **2021**, *16*, 034038. [CrossRef]

26. Wang, Y.; Wang, H.; Tan, W.; Huo, D. Magnetization reversal, critical behavior, and magnetocaloric effect in $NdMnO_3$: The role of magnetic ordering of Nd and Mn moments. *J. Appl. Phys.* **2022**, *132*, 183907. [CrossRef]

27. Cheng, C.; Dai, J.; Li, Z.; Feng, W. Preparation and magnetic properties of $CoFe_2O_4$ oriented fiber arrays by electrospinning. *Materials* **2020**, *13*, 3860–3870. [CrossRef]

28. Bahoosh, S.G.; Trimper, S.; Wesselinowa, J.M. Origin of ferromagnetism in $BaTiO_3$ nanoparticles. *Phys. Status Solidi RRL* **2011**, *5*, 382–384. [CrossRef]

29. Phan, T.; Zhang, P.; Yang, D.S.; Thanh, T.D.; Tuan, D.A.; Yu, S.C. Origin of ferromagnetism in $BaTiO_3$ nanoparticles prepared by mechanical milling. *J. Appl. Phys.* **2013**, *113*, 17E035. [CrossRef]

30. Mansourian, S.; Bakhshayeshi Ali Mendi, R.T. Giant magneto-impedance variation in amorphous CoFeSiB ribbons as a function of tensile stress and frequency. *Phys. Lett. A* **2020**, *384*, 126657. [CrossRef]

31. Corte-León, P.; Zhukova, V.; Ipatov, M.; Blanco, J.M.; Zhukov, A. Effect of Joule heating on giant magnetoimpedance effect and magnetic properties of Co-rich microwires. *J. Alloys Compd.* **2021**, *883*, 160778.